Eur. Phys. J. C 17, 663–673 (2000)
Digital Object Identifier (DOI) 10.1007/s100520000509

THE EUROPEAN PHYSICAL JOURNAL C

(3+1)-dimensional relativistic hydrodynamical expansion of hot and dense matter in ultra-relativistic nuclear collision

C. Nonaka[1,a], E. Honda[1], S. Muroya[2]

[1] Department of Physics, Hiroshima University, Higashi-Hiroshima 739-8526, Japan
[2] Tokuyama Women's College, Tokuyama, 745-8511, Japan

Received: 18 July 2000 / Published online: 23 October 2000 – © Springer-Verlag 2000

Abstract. A full (3+1)-dimensional calculation using Lagrangian hydrodynamics is proposed for relativistic nuclear collisions. This calculation enables us to evaluate the anisotropic flow of the hadronic matter which appears in non-central and/or asymmetrical relativistic nuclear collisions. Applying hydrodynamical calculations to the deformed uranium collisions in the AGS energy region, we discuss the nature of the space-time structure and particle distributions in detail.

1 Introduction

The study of the hot and dense matter which is produced in relativistic nuclear collisions has received intensive attention, and a number of experiments have been done to realize the phenomena [1]. The hydrodynamical model is one of the established models for describing the global features in relativistic nuclear collisions by collective flow. Recently, anisotropic flow phenomena have been observed at AGS [2,3] and also at SPS [4–6]. Several authors have argued the relation between the behavior of the collective flow and the equation of state. Based on the relativistic hydrodynamical model, Rischke reported that the existence of the minimum point in the excitation function of directed flow would suggest a phase transition [7]. Danielewicz has shown that the elliptic flow is sensitive to the differences of the nuclear equation of state by using a relativistic hadron transport model [8]. Sorge has discussed the centrality dependence of elliptic flow based on the event generator RQMD which includes a phase transition [5,9]. Hence, the analysis of the flow can inform us about the properties of the nuclear equation of state and of the quark–gluon plasma (QGP).

Since Bjorken proposed the scaling solution [10], a number of investigations based on the relativistic hydrodynamical model have been done. These successfully reproduced the experimental inclusive spectra at both AGS and SPS energy [11–17]. Ornik et al. investigated the single particle distribution and Bose–Einstein correlation at SPS [14]. Sollfrank et al. discussed the hadron spectra and the electromagnetic spectra at SPS [15]. Hung and Shuryak discussed the equation of state, radial flow, and freeze-out at AGS and SPS [16]. Morita et al. discussed the single particle distribution and Bose–Einstein correlation at SPS [18]. Therefore, the relativistic hydrodynamical model works well in the analyses of many kinds of phenomena in ultra-relativistic collisions. However, in most of the studies based on the relativistic hydrodynamical model, cylindrical symmetry is assumed and, therefore, the discussions are limited only to central collisions.

Recently, anisotropic flow has been analyzed by using the relativistic hydrodynamical model. Teaney and Shuryak proposed the "nutcracker" phenomenon [19] and Kolb et al. discussed anisotropic flow and the phase transition [20]. But these analyses use Bjorken's scaling solution in the longitudinal direction, and their discussion is restricted in the mid-rapidity region.

In order to investigate anisotropic flow, the quantitatively reliable (3+1)-dimensional relativistic hydrodynamical calculation is indispensable. The full (3+1)-dimensional calculation of the relativistic hydrodynamical equation has already been done by Rischke et al. [21] and Brachmann et al. [22]. Rischke pointed out that the minimum of the excitation function of the directed flow suggests the existence of a phase transition [21]. Brachmann et al. [22] discussed the antiflow of nucleons at the softest point of the equation of state using three-fluid dynamics. Their numerical schemes are based on the Eulerian hydrodynamics.

Here, we present the Lagrangian hydrodynamic simulation without assuming cylindrical symmetry, which makes the full (3+1)-dimensional analyses possible. The Lagrangian hydrodynamics has several advantages over the Eulerian hydrodynamics to investigate phenomena in ultra-relativistic nuclear collisions. As is well known, in the Lagrangian method grid points move along the flow, and is superior to the Eulerian approach when the calculation region varies rapidly. This is a great advantage for high energy collisions where the initial nuclei are Lorentz contracted. Secondly, we can follow a trajectory directly in the phase diagram in the case of a Lagrangian algorithm.

[a] e-mail: nonaka@butsuri.sci.hiroshima-u.ac.jp

$$
\begin{pmatrix}
\gamma^2 v_x & \gamma^2 v_y & \gamma^2 v_z & \frac{1}{\omega}\frac{\partial \epsilon}{\partial T} & \frac{1}{\omega}\frac{\partial \epsilon}{\partial \mu} \\
\gamma^2 & 0 & 0 & \frac{1}{\omega} v_x \frac{\partial p}{\partial T} & \frac{1}{\omega} v_x \frac{\partial p}{\partial \mu} \\
0 & \gamma^2 & 0 & \frac{1}{\omega} v_y \frac{\partial p}{\partial T} & \frac{1}{\omega} v_y \frac{\partial p}{\partial \mu} \\
0 & 0 & \gamma^2 & \frac{1}{\omega} v_z \frac{\partial p}{\partial T} & \frac{1}{\omega} v_z \frac{\partial p}{\partial \mu} \\
n_B \gamma^2 v_x & n_B \gamma^2 v_y & n_B \gamma^2 v_z & \frac{\partial n_B}{\partial T} & \frac{\partial n_B}{\partial \mu}
\end{pmatrix} \partial_t
\begin{pmatrix} v_x \\ v_y \\ v_z \\ T \\ \mu \end{pmatrix}
$$

$$
+ \begin{pmatrix}
\gamma^2 v_x^2 + 1 & \gamma^2 v_x v_y & \gamma^2 v_x v_z & \frac{1}{\omega} v_x \frac{\partial \epsilon}{\partial T} & \frac{1}{\omega} v_x \frac{\partial \epsilon}{\partial \mu} \\
\gamma^2 v_x & 0 & 0 & \frac{1}{\omega}\frac{\partial p}{\partial T} & \frac{1}{\omega}\frac{\partial p}{\partial \mu} \\
0 & \gamma^2 v_x & 0 & 0 & 0 \\
0 & 0 & \gamma^2 v_x & 0 & 0 \\
n_B(\gamma^2 v_x^2 + 1) & n_B \gamma^2 v_x v_y & n_B \gamma^2 v_x v_z & n_B \frac{\partial n_B}{\partial T} & n_B \frac{\partial n_B}{\partial \mu}
\end{pmatrix} \partial_x
\begin{pmatrix} v_x \\ v_y \\ v_z \\ T \\ \mu \end{pmatrix}
$$

$$
+ \begin{pmatrix}
\gamma^2 v_y v_x & \gamma^2 v_y^2 + 1 & \gamma^2 v_y v_z & \frac{1}{\omega} v_y \frac{\partial \epsilon}{\partial T} & \frac{1}{\omega} v_y \frac{\partial \epsilon}{\partial \mu} \\
\gamma^2 v_y & 0 & 0 & 0 & 0 \\
0 & \gamma^2 v_y^2 & 0 & \frac{1}{\omega}\frac{\partial p}{\partial T} & \frac{1}{\omega}\frac{\partial p}{\partial \mu} \\
0 & 0 & \gamma^2 v_y 0 & 0 & \\
n_B \gamma^2 v_y v_x & n_B(\gamma^2 v_y^2 + 1) & n_B \gamma^2 v_y v_x & v_y \frac{\partial n_B}{\partial T} & v_y \frac{\partial n_B}{\partial \mu}
\end{pmatrix} \partial_y
\begin{pmatrix} v_x \\ v_y \\ v_z \\ T \\ \mu \end{pmatrix}
$$

$$
+ \begin{pmatrix}
\gamma^2 v_z v_x & \gamma^2 v_z v_y & \gamma^2 v_z^2 + 1 & \frac{1}{\omega} v_z \frac{\partial \epsilon}{\partial T} & \frac{1}{\omega} v_z \frac{\partial \epsilon}{\partial \mu} \\
\gamma^2 v_z & 0 & 0 & 0 & 0 \\
0 & \gamma^2 v_z & 0 & 0 & 0 \\
0 & 0 & \gamma^2 v_z & \frac{1}{\omega}\frac{\partial p}{\partial T} & \frac{1}{\omega}\frac{\partial p}{\partial \mu} \\
n_B \gamma^2 v_z v_x & n_B \gamma^2 v_z v_y & n_B(\gamma^2 v_z^2 + 1) & v_z \frac{\partial n_B}{\partial T} & v_z \frac{\partial n_B}{\partial \mu}
\end{pmatrix} \partial_z
\begin{pmatrix} v_x \\ v_y \\ v_z \\ T \\ \mu \end{pmatrix}
$$

$$
= 0, \tag{5}
$$

This allows us to study heavy ion collision phenomena together with the equation of state.

As an example of the anisotropic flow in heavy ion collisions, we apply our hydrodynamical model to deformed uranium–uranium collisions at AGS energy and analyze the elliptic flow in detail. Shuryak pointed out the remarkable features of the deformed uranium collisions which are suitable for the important problems such as hard processes, elliptic flow, and J/ψ suppression [23]. The effect of such a deformation on the flow [24] and J/Ψ suppression [25] has been investigated. Here, we discuss the influence of the deformation of a uranium nucleus on elliptic flow.

In Sect. 2 we introduce the relativistic hydrodynamical equation and explain our original algorithm of the numerical calculation of the (3+1)-dimensional relativistic hydrodynamical equation. In Sect. 3 we apply our hydrodynamical model to the investigation of elliptic flow which is produced in deformed uranium collisions and discuss the effect of the deformation on elliptic flow in detail. Section 4 is devoted to a summary of this paper.

2 Algorithm to solve the hydrodynamical equation

2.1 Relativistic hydrodynamical equation

The relativistic hydrodynamical equation in Lorentz covariant form is

$$
\partial_\mu T^{\mu\nu} = 0. \tag{1}
$$

Since we discuss a system formed by nuclear collisions, baryon number current conservation should also be taken into account,

$$
\partial_\nu j_B^\nu = 0. \tag{2}
$$

In this paper, $T^{\mu\nu}$ is taken as the energy-momentum tensor of the perfect fluid,

$$
T^{\mu\nu} = \epsilon u^\mu u^\nu - p(g^{\mu\nu} - u^\mu u^\nu), \tag{3}
$$

and the baryon number current is given by

$$
j_B^\nu = n_B(T, \mu) u^\nu. \tag{4}
$$

Here ϵ, p and n_B are energy density, pressure and baryon number density, respectively. These are the functions of the coordinates through the temperature $T(x_\mu)$ and the baryon number chemical potential $\mu(x_\mu)$. $u^\mu = \gamma(1, v_x, v_y, v_z)$ and $g^{\mu\nu} = \mathrm{diag.}(1, -1, -1, -1)$ are the local four-velocity and metric tensor, respectively. If the equation of state is properly given, we can solve the coupled equations (1) and (2) and obtain the chronological evolution of the temperature and the chemical potential. In order to make our numerical method clear, (1) and (2) are rewritten as (see (5) on top of the page) where $\gamma = 1/(1 - v^2)^{1/2}$, $\omega = \epsilon + p$. From the time-like projection of (1), $u^\nu \partial_\mu T^{\mu\nu} = 0$, and (2), one can obtain the entropy conservation law,

$$
\partial^\mu s_\mu = 0, \tag{6}
$$

with the aid of the thermodynamical relation

$$\epsilon + p = Ts + \mu n_B, \tag{7}$$

where $s^\mu = su^\mu$ is the entropy current density. We numerically solve (2) and (6) with the algorithm which will be explained in the next subsection.

2.2 Computational scheme

Most hydrodynamic calculations which are used for investigating the various phenomena in heavy ion collisions are based on the Eulerian hydrodynamics. Sollfrank et al. analyze the hadron and electromagnetic spectra by using the SHASTA algorithm [15]. The HYLANDER and HYLANDER-C algorithm are used by Ornik et al. [14] and Schlei and Strottman [17], respectively. Rischke et al. use the RHHLE algorithm and study hydrodynamics and collective flow [7].

Here, we solve the (3+1)-dimensional relativistic hydrodynamical equation with Lagrangian hydrodynamics. Lagrangian hydrodynamics has several advantages over Eulerian hydrodynamics in treating ultra-relativistic nuclear collisions. At high energies, the initial distribution of the energy localizes due to collision of the Lorentz contracted projectile and target. To treat the situation, a fine resolution is required in the Eulerian hydrodynamics and computational cost becomes great. On the other hand, in Lagrangian hydrodynamics, discretized grids move along the expansion of the fluid; therefore, we can perform the calculation at all stages on the lattice points which we prepare under the initial conditions. For example, in our previous calculation [26] the fluid expands four times larger in the longitudinal direction. This fact means we need the four-times larger number of grid points in the longitudinal direction if we use the naive Euler type algorithm. Another merit of the Lagrangian hydrodynamics is that it enables us to derive the physical information directly, because it follows the flux of the current. For example, the path of a volume element of fluid in the T–μ plane can be traced, as we will demonstrate in the next subsection. Therefore, we are able to discuss how the phase between hadron phase and QGP phase affects the physical phenomena by the Lagrangian hydrodynamics.

Our numerical calculation of the (3+1)-dimensional relativistic hydrodynamical equation is as follows: First, the coordinate at time $t + \Delta t$, $x^m = X^m(t,i,j,k)$, is evolved as

$$X^m(t+\Delta t,i,j,k) = X^m(t,i,j,k) + \frac{u^m(t,i,j,k)}{u^t(t,i,j,k)}\Delta t. \tag{8}$$

By definition of the Lagrangian hydrodynamics, the coordinates move in parallel with j^μ and s^μ.

Second, the local velocity is determined:

$$\begin{aligned} &v^m(t+\Delta t,i,j,k) = v^m(t,i,j,k) + \partial_t v^t(i,j,k,t)\Delta t \\ &+\sum_{n=1}^{3} \partial_n v^m(i,j,k,t)(X^n(t+\Delta t,i,j,k) \\ &-X^n(t,i,j,k)), \end{aligned} \tag{9}$$

where the value of $\partial^\mu v_\mu$ is obtained from (5).

Finally, the temperature and chemical potential are derived. The volume element $\mathrm{d}\sigma^\mu$ at time t is surrounded by eight points, $X^\mu(t,i,j,k)$, $X^\mu(t,i+1,j,k)$, $X^\mu(t,i,j+1,k)$, $X^\mu(t,i,j,k+1)$, $X^\mu(t,i+1,j+1,k)$, $\cdots$, $X^\mu(t,i+1,j+1,k+1)$. Using this volume element, (2) and (6) are rewritten as

$$\begin{aligned} &s(T(t+\Delta t,i,j,k),\mu(t+\Delta t,i,j,k)) \\ &\times u^t(t+\Delta t,i,j,k)\mathrm{d}\sigma_t(t+\Delta t,i,j,k) \\ &= s(T(t,i,j,k),\mu(t,i,j,k))u^t(t,i,j,k) \\ &\times \mathrm{d}\sigma_t(t,i,j,k), \end{aligned} \tag{10}$$

$$\begin{aligned} &n_B(T(t+\Delta t,i,j,k),\mu(t+\Delta t,i,j,k)) \\ &\times u^t(t+\Delta t,i,j,k)\mathrm{d}\sigma_t(t+\Delta t,i,j,k) \\ &= n_B(T(t,i,j,k),\mu(t,i,j,k))u^t(t,i,j,k) \\ &\times \mathrm{d}\sigma_t(t,i,j,k). \end{aligned} \tag{11}$$

Here, by virtue of the determination of coordinates (8), we can use the relation,

$$u^\mu \mathrm{d}\sigma_\mu = u^t \mathrm{d}\sigma_t.$$

Since s and n_B depend on T and μ, using up to first order differences of the temperature, $\Delta T(t,i,j,k) \equiv T(t+\Delta t,i,j,k) - T(t,i,j,k)$, and of the chemical potential, $\Delta\mu(t,i,j,k) \equiv \mu(t+\Delta t,i,j,k) - \mu(t,i,j,k)$, we expand s and n_B as

$$\begin{aligned} &s(T(t+\Delta t,i,j,k),\mu(t+\Delta t,i,j,k)) \\ &= s(T(t,i,j,k),\mu(t,i,j,k)) \\ &+\left[\frac{\partial s}{\partial T}\right]_{\substack{T=T(t,i,j,k)\\ \mu=\mu(t,i,j,k)}} \Delta T + \left[\frac{\partial s}{\partial \mu}\right]_{\substack{T=T(t,i,j,k)\\ \mu=\mu(t,i,j,k)}} \Delta\mu, \end{aligned} \tag{12}$$

$$\begin{aligned} &n_B(T(t+\Delta t,i,j,k),\mu(t+\Delta t,i,j,k)) \\ &= n_B(T(t,i,j,k),\mu(t,i,j,k)) \\ &+\left[\frac{\partial n_B}{\partial T}\right]_{\substack{T=T(t,i,j,k)\\ \mu=\mu(t,i,j,k)}} \Delta T + \left[\frac{\partial n_B}{\partial \mu}\right]_{\substack{T=T(t,i,j,k)\\ \mu=\mu(t,i,j,k)}} \Delta\mu. \end{aligned} \tag{13}$$

Substituting (12) and (13) into (10) and (11), we obtain the temperature and chemical potential at the next time step,

$$\begin{aligned} &T(t+\Delta t,i,j,k) = T(t,i,j,k) \\ &+\frac{1}{\Delta_{s,n_B}}\left\{\frac{\partial n_B}{\partial \mu}s(T,\mu) - \frac{\partial s}{\partial \mu}n_B(T,\mu)\right\}\Bigg|_{\substack{T=T(t,i,j,k)\\ \mu=\mu(t,i,j,k)}} [\cdots], \end{aligned} \tag{14}$$

$$\begin{aligned} &\mu(t+\Delta t,i,j,k) = \mu(t,i,j,k) \\ &+\frac{1}{\Delta_{s,n_B}}\left\{\frac{\partial n_B}{\partial T}n_B(T,\mu) - \frac{\partial s}{\partial T}s(T,\mu)\right\}\Bigg|_{\substack{T=T(t,i,j,k)\\ \mu=\mu(t,i,j,k)}} [\cdots], \end{aligned} \tag{15}$$

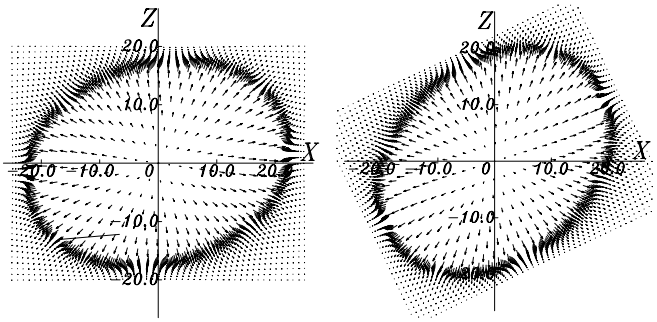

Fig. 1. The left part of the figure indicates the flow at $y \sim 0$ fm and $t = 20$ fm/c in an Au + Au 10.8 AGeV collision [26]. The right part of the figure shows the same result which is obtained by the calculation with the grids rotated 26 degrees on the x–z plane

where Δ_{s,n_B} and $[\cdots]$ are

$$\Delta_{s,n_B} = \left(\frac{\partial s(T,\mu)}{\partial T} \frac{\partial n_B(T,\mu)}{\partial \mu} - \frac{\partial s(T,\mu)}{\partial \mu} \frac{\partial n_B(T,\mu)}{\partial T} \right) \Bigg|_{\substack{T=T(t,i,j,k) \\ \mu=\mu(t,i,j,k)}},$$

$$[\cdots] = \left[\frac{u^t(t,i,j,k)\mathrm{d}\sigma^t(t,i,j,k)}{u^t(t+\Delta t,i,j,k)\mathrm{d}\sigma^t(t+\Delta t,i,j,k)} - 1 \right],$$

respectively. These numerical procedures are the extension of the method in [12].

In this algorithm the CPU time is almost proportional to the number of lattice points. A numerical calculation of the relativistic hydrodynamical equation in this paper has been performed at the Institute for Nonlinear Sciences and Applied Mathematics, Hiroshima University. Average floating point operations for $(55, 63, 49)$ space points and 5300 time steps are 36 Tera in each calculation reported in the next section.

In order to analyze anisotropic flow with high accuracy, the artificial anisotropy which can be caused by the discretization of space should be small. We checked the reliability of our calculation by comparing the results with a rotated spatial grid. Figure 1 shows the results of the flow obtained by a different choice of the grid. The difference of flow between the two results is less than 0.15% in the present calculations.

2.3 Path in the phase diagram

The Lagrangian hydrodynamics enables us to easily trace the history of the trajectory of the flux. In order to test the applicability of our algorithm in the study of the chronological trajectory of the volume element in the phase diagram, we use the equation of state which contains the first order phase transition only in this subsection. Above the phase transition, the thermodynamical quantities are assumed to be determined by QGP gas which is dominated by massless u, d, s quarks and gluons. In the QGP phase the pressure is given by

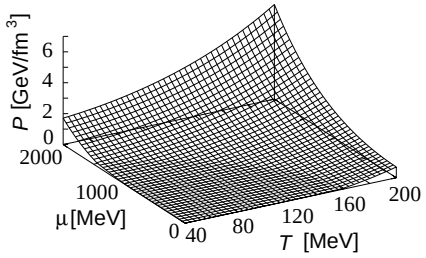

Fig. 2. The equation of state including the first order phase transition

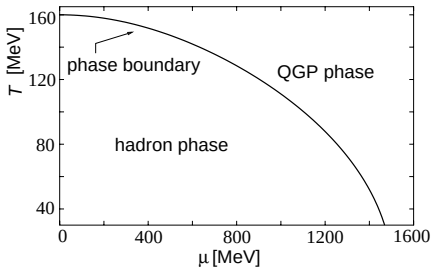

Fig. 3. The phase boundary which is determined by the pressure balance

$$p = \frac{(32+21N_f)\pi^2}{180}T^4 + \frac{N_f}{2}\left(\frac{\mu}{3}\right)^2 T^2 + \frac{N_f}{4\pi^2}\left(\frac{\mu}{3}\right)^4 - B, \tag{16}$$

where N_f is 3 and B is the Bag constant [15,16]. For the hadron phase we use the excluded volume model [27] which contains all resonances up to 2.0 GeV [28]. In the hadron phase the fermion pressure is given by

$$p^{\mathrm{excl}}(T,\{\mu_i\}) = \sum_i p_i^{\mathrm{ideal}}\left(T, \mu_i - V_0 p^{\mathrm{excl}}(T,\{\mu_i\})\right) = \sum_i p_i^{\mathrm{ideal}}(T,\tilde{\mu_i}), \tag{17}$$

where p^{ideal} is the pressure of an ideal hadron gas and V_0 is the excluded volume of which the radius is fixed to 0.7 fm. Putting the critical temperature to 160 MeV for zero chemical potential, the Bag constant, $B^{1/4}$, is given by 233 MeV. Figure 2 shows the equation of state as a function of the temperature and the chemical potential. Figure 3 indicates the phase boundary which is determined by the pressure balance between the two phases, i.e., $p_Q = p_H$. In the mixed phase we introduce the fraction of the volume of the QGP phase, $\lambda(x_\mu)$ $(0 \le \lambda \le 1)$ and parameterize energy density and baryon number density by

$$\begin{aligned} \epsilon_M(\lambda, T^*(\mu)) &= \lambda\epsilon_Q(T^*(\mu)) - (1-\lambda)\epsilon_H(T^*(\mu)), \\ n_{BM}(\lambda, T^*(\mu)) &= \lambda n_{BQ}(T^*(\mu)) - (1-\lambda)n_{BH}(T^*(\mu)), \end{aligned} \tag{18}$$

where $T^*(\mu)$ is the value of the temperature on the phase boundary in the phase diagram. Contrary to the Eulerian

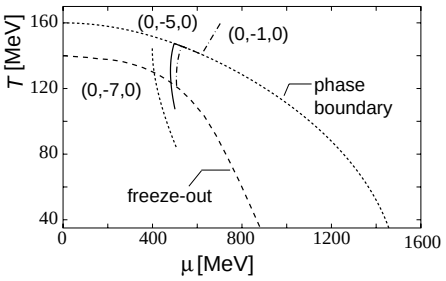

Fig. 4. The paths in the phase diagram. The dot-dashed line stands for the path which starts from the QGP phase and on this line n_B/s is 0.065. The solid line stands for the path which starts from the mixed phase, and on this line n_B/s is 0.059. The dotted line stands for the path which starts from the hadron phase, and on this line n_B/s is 0.044

hydrodynamics, where the boundary condition should be considered on the discontinuous plane between two phases [29,30], in our algorithm, by virtue of the explicit use of the current conservation equations, the flux of the fluid can be traced easily even if the discontinuity of the thermodynamical quantities caused by the first order phase transition exists [18,31]. For the initial conditions, we use the results which are obtained by URASiMA (Ultra-Relativistic A–A collision Simulator based on Multiple scattering Algorithm) in Au+Au 20 AGeV collisions [26].

Figure 4 shows the typical paths in the phase diagram. For instance, the trajectory of the volume element of the grid number $(x, y, z) = (0, -1, 0)$, which starts from the QGP region, moves along the phase boundary before entering the hadron phase. The volume element of $(0, -5, 0)$, which starts from the mixed phase, also moves along the phase boundary before turning into the hadron phase. On the other hand the volume element of the grid number $(x, y, z) = (0, -7, 0)$, which starts from the hadron phase, draws a smooth trajectory to the freeze-out. This behavior is the same result as discussed in [16]. By virtue of the Lagrangian hydrodynamics we can easily trace the trajectory which corresponds to the adiabatic paths in the T–μ plane.

3 Effect of deformed uranium on collective flow

As an application of our hydrodynamical model, we investigate the flow which is generated in the deformed uranium collisions. Shuryak has pointed out that remarkable problems such as hard processes, elliptic flow, and the mechanism of J/ψ suppression can be resolved by using the deformed uranium collisions [23]. Since Danielewicz showed that elliptic flow is sensitive to the nuclear equation of state at AGS energy [8], the elliptic flow is one of the hottest topics in high energy nuclear physics. The high accuracy experiments for elliptic flow have been done at AGS [2,3] and SPS [4–6]. Recently, using the cascade model of the ART, Li discussed the elliptic flow in deformed uranium collisions [24]. If the deformation has a large influence on the anisotropic flow, the analyses of collective flow using U+U collisions are promising for investigating the difference between QGP states and hadron states. In order to analyze anisotropic flow of deformed uranium collisions, the (3+1)-dimensional relativistic hydrodynamical model plays a central role, i.e. it provides us with reliable quantitative results.

Here, the ellipticity is measured by the asymmetry of the azimuthal particle distribution which is expanded based on the Fourier series:

$$\frac{\mathrm{d}N}{\mathrm{d}\phi} \sim v_0(1 + 2v_1\cos(\phi) + 2v_2\cos(2\phi)), \qquad (19)$$

where ϕ is the azimuth and v_0 is the normalization. The parameters v_1 and v_2 correspond to the intensity of the directed flow and elliptic flow, respectively.

The shape of the deformed uranium nucleus is approximately ellipsoid, and the short (R_t) and long (R_c) semi-axis are given by

$$R_t = R_s\left(1 - \frac{1}{3}\delta\right),$$
$$R_c = R_s\left(1 + \frac{2}{3}\delta\right), \qquad (20)$$

where $\delta = 0.27$ is the deformation parameter [32]. We will investigate how the deformation and the orientation between two colliding deformed uranium nuclei influence the flow of the hadrons produced. Among the many types of collisions, as to the orientation we focus on two types, i.e., tip–tip collisions in which the long axes of two nuclei are along the beam direction, and body–body collisions in which the long axes of two nuclei are parallel to each other but perpendicular to the beam direction. We also calculate sphere–sphere collisions for comparison.

3.1 Model description

In outline our calculation procedure is as follows: First, we parameterize the initial conditions of energy density, baryon number density and local velocity based on the result of event generator URASiMA.

Our event generator URASiMA [33–35] is characterized by the multi-chain model (MCM) by which the multiparticle production process can be successfully described. In URASiMA the detailed balance between quasi-two-body production and absorption processes holds. It is applicable to the AGS and SPS energy regions and the calculated results reproduce the experimental data of the hadron spectra [33]. Recently, the thermodynamical properties of hot and dense hadronic gas were also investigated by URASiMA [34,35]. For a more detailed discussion, see [33–35].

In order to solve the relativistic hydrodynamical equation, we need to introduce an equation of state. Since our calculation does not rely on any artificial assumption, we can investigate how the difference of the equations of state has an effect on the physical phenomena. For the first trial,

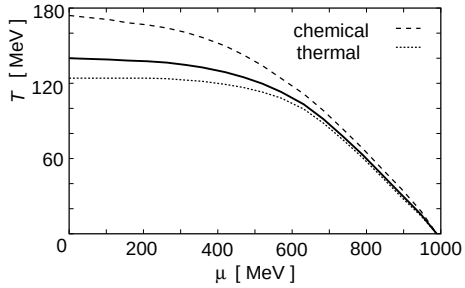

Fig. 5. The freeze-out condition. The solid line stands for the freeze-out condition which is determined from the thermal freeze-out (the dotted line) and the chemical freeze-out (the dashed line)

we adopt the equation of state of the ideal hadron gas including resonances; this is the same equation of state as we used for the initial conditions. The temperature and chemical potential of the volume elements vary with the space-time evolution of the fluid until the hadronization process occurs.

Finally, hadron spectra are obtained by the Cooper–Frye formula [36]. We assume that the hadronization process occurs when the temperature and chemical potential of the volume elements cross the boundary (the solid line in Fig. 5). The solid line is obtained so that the freeze-out temperature becomes 140 MeV at vanishing chemical potential, based on the chemical freeze-out model and the thermal freeze-out model [37]. Using the Cooper–Frye formula the particle distribution is given by

$$E\frac{\mathrm{d}N}{\mathrm{d}^3P} = \sum_h \frac{g_h}{(2\pi)^3}\int_\sigma \mathrm{d}\sigma_\mu P^\mu \times \frac{1}{\exp[(P_\nu u^\nu - \mu_\mathrm{f})/T_\mathrm{f}] \pm 1}, \tag{21}$$

where g_h is the degeneracy of the hadrons and T_f and μ_f are the freeze-out temperature and chemical potential shown in Fig. 5, respectively, and u^μ is the local velocity of the fluid on the hypersurface $\mathrm{d}\sigma_\mu$.

We determine the hypersurface $\mathrm{d}\sigma_\mu$ by evaluating the normal vector to the freeze-out hypersurface [38]. We evaluate the intensity of the elliptic flow v_2 using (19) and (21).

3.2 Initial conditions

In high energy collisions such as SPS and RHIC, the contribution of the spectator to the initial conditions is small and "in-plane" elliptic flow is enhanced [39]. However, if we focus on the AGS energy regions in which the incident energy is not so large, the effect of the deformation can remain strong. In order to prepare the appropriate initial conditions, we estimate the energy density distribution and baryon number density distribution by the event generator URASiMA. We calculate the space-time evolution in U+U 10 AGeV and 20 AGeV tip–tip, body–body and sphere–sphere collisions at $b = 0$ and 6 fm, using the event generator URASiMA, where b is the impact parameter. In the case of tip–tip and body–body collisions, we consider the collision of the deformed uranium according to (20). We assume that the hydrodynamical expansion starts when the projectile nucleus finishes passing through the target nucleus. At this time the initial conditions of the hydrodynamical model, $T(x_\mu)$, $\mu(x_\mu)$, and $u^\mu(x_\mu)$, should be given.

The results of URASiMA are listed in Tables 1a (U+U 10 AGeV) and 1b (U+U 20 AGeV). In a body–body collision the energy density and baryon number density are the smallest among the different types of collision for the same incident energy and impact parameter. For tip–tip collisions the decrease in the energy density and baryon density with impact parameter is the largest among the three types of collision. Next the initial energy density distribution and baryon number density distribution are parametrized based on these data in Tables 1a and 1b. The initial energy density and baryon number density distributions are given by

$$\begin{aligned}\epsilon &= \epsilon_\mathrm{max} B(x,y,z),\\ n_B &= n_{B\mathrm{max}} B(x,y,z),\end{aligned} \tag{22}$$

where $B(x,y,z)$ is the distribution function, which is determined so that the result of URASiMA is reproduced, and ϵ_max and $n_{B\mathrm{max}}$ are the values of the result of URASiMA in the central region. We interpolate and/or extrapolate the values of ϵ_max and $n_{B\mathrm{max}}$ from the data of Tables 1a and 1b as follows. The distribution function is given by

$$\begin{aligned}B(x,y,z) = \frac{1}{c_1}\Bigg[&a_1 \exp\left(-\frac{(x-x_\mathrm{cs})^2}{\sigma_{\mathrm{s}x}^2} - \frac{(y-y_\mathrm{cs})^2}{\sigma_{\mathrm{s}y}^2} - \frac{(z-z_\mathrm{cs})^2}{\sigma_{\mathrm{s}z}^2}\right)\\ &+a_1 \exp\left(-\frac{(x+x_\mathrm{cs})^2}{\sigma_{\mathrm{s}x}^2} - \frac{(y+y_\mathrm{cs})^2}{\sigma_{\mathrm{s}y}^2} - \frac{(z+z_\mathrm{cs})^2}{\sigma_{\mathrm{s}z}^2}\right)\\ &+\exp\left(-\frac{(x-x_\mathrm{cp})^2}{\sigma_{\mathrm{p}x}^2} - \frac{(y-y_\mathrm{cp})^2}{\sigma_{\mathrm{p}y}^2} - \frac{(z-z_\mathrm{cp})^2}{\sigma_{\mathrm{p}z}^2}\right)\Bigg],\end{aligned} \tag{23}$$

where c_1 is the normalization, and the parameter which corresponds to the ratio of the energy density of the spectator to that of the participant, a_1, is fixed to be 0.7 for all cases. The ratio of the baryon number density is also fixed by a_1. In (23) x_cp, y_cp, and z_cp are the center of participant, and x_cs, y_cs and z_cs are the center of spectator. Their specific values are determined geometrically by the position of the projectile nucleus and target nucleus. For the participant,

$$\begin{aligned}x_\mathrm{cp} &= y_\mathrm{cp} = z_\mathrm{cp} = 0,\\ \sigma_{\mathrm{p}x} &= a_3\left(R_x - \frac{b}{2}\right),\\ \sigma_{\mathrm{p}y} &= \frac{R_y}{R_x}\sqrt{R_x^2 - \frac{b^2}{4}},\\ \sigma_{\mathrm{p}z} &= a_4\frac{z_\mathrm{cs}}{\gamma}.\end{aligned} \tag{24}$$

Table 1. The energy and baryon number densities obtained by URASiMA at $(x, y, z) = (0, 0, 0)$ for different types of collisions and the impact parameters. **a** U+U 10 AGeV, **b** U+U 20 AGeV

Table 1a: The result of URASiMA (U+U 10.0 AGeV)

b [fm]	Type of collision	Initial time [fm/c]	ϵ [GeV/fm^3] at $(0,0,0)$	n_B [fm^{-3}] at $(0,0,0)$
0	tip–tip	8.5	1.975	0.977
6	tip–tip	8.5	1.403	0.718
0	sphere–sphere	7.0	1.807	0.929
6	sphere–sphere	7.0	1.611	0.809
0	body–body	6.5	1.681	0.819
6	body–body	6.5	1.490	0.728

Table 1b: The result of URASiMA (U+U 20.0 AGeV)

b [fm]	Type of collision	Initial time [fm/c]	ϵ [GeV/fm^3] at $(0,0,0)$	n_B [fm^{-3}] at $(0,0,0)$
0	tip–tip	6.0	2.871	1.124
6	tip–tip	6.0	2.060	0.825
0	sphere–sphere	5.0	2.744	1.064
6	sphere–sphere	5.0	2.241	0.869
0	body–body	4.5	2.248	0.933
6	body–body	4.5	2.253	0.860

For the spectator,

$$
\begin{aligned}
x_{\rm cs} &= \frac{R_x}{2} + \frac{b}{4}, \\
y_{\rm cs} &= 0, \\
z_{\rm cs} &= t_{\rm i} - \frac{R_z}{\gamma}, \\
\sigma_{{\rm s}x} &= a_5 \frac{b}{2}, \\
\sigma_{{\rm s}y} &= \begin{cases} R_x & (b \geq R_x), \\ \dfrac{R_y}{R_x}\sqrt{2R_x b - b^2} & (b \leq R_x), \end{cases} \\
\sigma_{{\rm s}z} &= a_6 \frac{R_z}{R_y \gamma}.
\end{aligned} \tag{25}
$$

R_x, R_y, and R_z are the radius of the projectile nucleus and the target nucleus in the x, y, and z directions. In a body–body collision, the x direction and y direction denote the longer axis and the shorter axis, respectively. In (25) $t_{\rm i}$ is the initial time when the hydrodynamical evolution starts. In (24) and (25), the parameters $a_3 \sim a_6$ are tuned so that the energy density and baryon number density distribution, (22), reproduce the result of URASiMA. The parameters $a_3 \sim a_6$ are fixed at 0.7, 2.5, 1.3, 0.7, respectively.

Figure 6 shows the energy density distribution of the initial conditions for U+U 20 AGeV sphere–sphere collisions at $b = 4.0$ fm. From this figure we can see clearly the contribution from the participant and the spectator. For the initial velocity distribution we neglect the transverse flow because its value is small in the result of URASiMA.

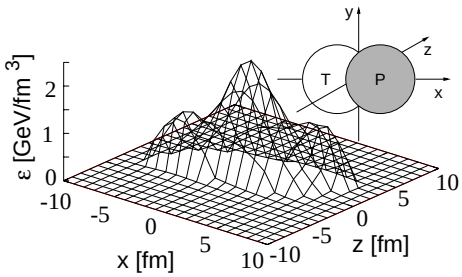

Fig. 6. The initial condition of the energy density distribution at $y = 0$ fm in a U+U 20 AGeV, sphere–sphere collision. In this case the impact parameter is 4.0 fm

The initial flow distribution is given by

$$
\begin{aligned}
v_x(x, y, z) &= 0, \\
v_y(x, y, z) &= 0, \\
v_z(x, y, z) &= \frac{z}{t} B_v(x, y, z).
\end{aligned} \tag{26}
$$

Here the distribution function $B_v(x, y, z)$ is given by

$$
\begin{aligned}
B_v(x, y, z) = \frac{1}{c_2} \Bigg[& \exp\left(-\frac{(x - x_{\rm cs})^2}{\sigma_{{\rm s}x}^2} \right. \\
& \left. - \frac{(y - y_{\rm cs})^2}{\sigma_{{\rm s}y}^2} - \frac{(z - z_{\rm cs})^2}{\sigma_{{\rm s}z}^2} \right) \\
& + \exp\left(-\frac{(x + x_{\rm cs})^2}{\sigma_{{\rm s}x}^2} - \frac{(y + y_{\rm cs})^2}{\sigma_{{\rm s}y}^2} - \frac{(z + z_{\rm cs})^2}{\sigma_{{\rm s}z}^2} \right) \\
& + a_2 \exp\left(-\frac{(x - x_{\rm cp})^2}{\sigma_{{\rm p}x}^2} - \frac{(y - y_{\rm cp})^2}{\sigma_{{\rm p}y}^2} \right.
\end{aligned}
$$

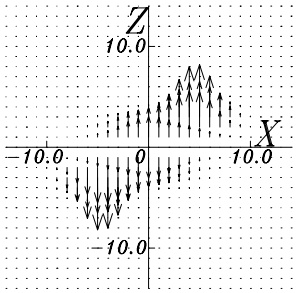

Fig. 7. The initial condition of the velocity distribution at $y = 0$ fm under the same conditions as Fig. 6

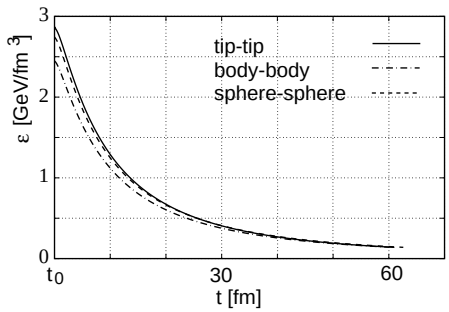

Fig. 8. The time evolution of the energy density of the central region in U+U 20 AGeV with $b = 0$ fm. The solid line, the dot-dashed line, and the dashed line stand for tip–tip collisions, body–body collisions, and sphere–sphere collisions, respectively

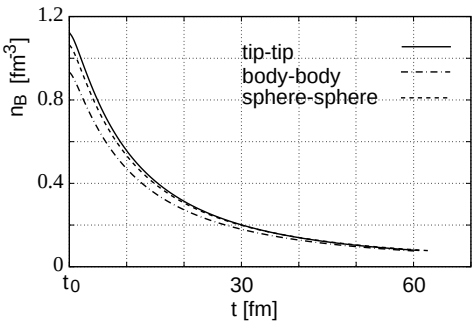

Fig. 9. The time evolution of the baryon number density distribution in the same case as Fig. 8. The solid line, the dot-dashed line, and the dashed line stand for tip–tip collisions, body–body collisions, and sphere–sphere collisions, respectively

$$- \frac{(z - z_{\rm cp})^2}{\sigma_{pz}^2}\Bigg)\Bigg], \tag{27}$$

where c_2 is the normalization and a_2 is the parameter, fixed at 1.4. Figure 7 shows the initial velocity distribution in the same case as Fig. 6. The flow in the longitudinal direction is similar to Bjorken's scaling solution in the central region.

3.3 Calculated results

Figures 8 and 9 indicate the expansion of the energy density and baryon number density in the central region.

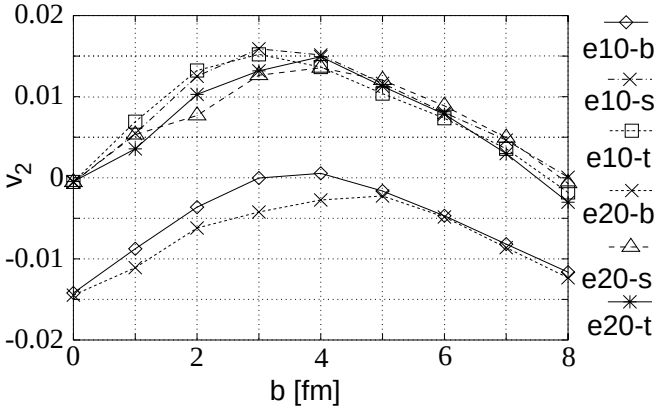

Fig. 10. The behavior of v_2 as a function of the impact parameter in all cases. In this figure e10-b means that the incident energy is 10 AGeV in body–body collisions, e10-s means that the incident energy is 10 AGeV in sphere–sphere collisions and e20-t means that the incident energy is 20 AGeV in tip–tip collisions, and so on

There is a slight difference in the life time in each case. The initial energy density and baryon number density of body–body collisions are the smallest among all three types of collisions and the difference between tip–tip and sphere–sphere collisions is small. At the initial time the difference of the energy density among all three types of collisions is $\Delta\epsilon \simeq 10 \sim 20\%$ and the time difference is $\Delta t \simeq 10 \sim 20\%$ at $\epsilon = 1\,\mathrm{GeV/fm^3}$. However, these kinds of differences among the collision types do not appear at the final time.

Figure 10 shows the behavior of v_2 of the nucleon as a function of the impact parameter for each type of collision at 10 and 20 AGeV. The elliptic flow parameter, v_2, increases with impact parameter and reaches a peak at $b = 3 \sim 4$ fm and decreases in every case. Furthermore, for body–body collisions v_2 does not vanish at $b = 0$. Consequently, the effect of the deformation is not negligible. In order to make this characteristic behavior clear we focus on the pressure distribution.

Figure 11 displays the pressure distribution in U+U 10 AGeV sphere–sphere collisions. From the figures at $z \sim 0$ fm we can see that the pressure gradient in the y direction increases with the impact parameter. Therefore one might consider that v_2 increases with impact parameter, because the velocity of the produced particles in the x direction is larger than the one in the y direction. But Fig. 10 shows that the value of v_2 starts to decrease at about $b = 3 \sim 4$ fm. Here we focus on the pressure distribution in the z plane in Fig. 11, and we can see that the effect of the spectator increases with the impact parameter. Because the spectators block the flow in the x direction, the growth of the flow in the x direction is suppressed. Consequently the behavior of v_2 is determined by both the pressure gradient and the effect of the spectator.

Figure 12 shows the pressure distribution at a U+U 20 AGeV collision at $b = 4.0$ fm. In the z plane there is a slight difference between tip–tip collisions and sphere–sphere collisions. On the other hand, in body–body collisions the extension of the pressure distribution in the x

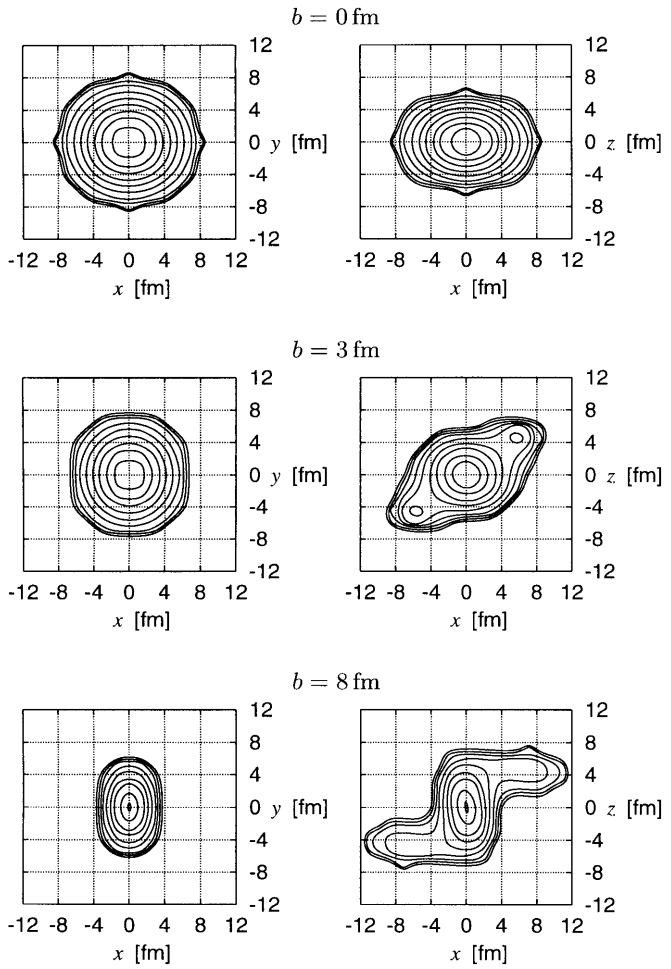

Fig. 11. The impact parameter dependence of the pressure distribution in U+U 10 AGeV sphere–sphere collisions at $t = 20\,\mathrm{fm}/c$. The left part of the figures displays the results at $z \sim 0\,\mathrm{fm}$ and the right part of the figures displays those at $y \sim 0\,\mathrm{fm}$. The highest values of the pressure distribution contours are $0.055\,\mathrm{GeV/fm^3}$ for $b = 0\,\mathrm{fm}$, $0.05\,\mathrm{GeV/fm^3}$ for $b = 3$ and 8 fm, respectively and the contour lines are drawn in steps of $\Delta p = 0.005\,\mathrm{GeV/fm^3}$

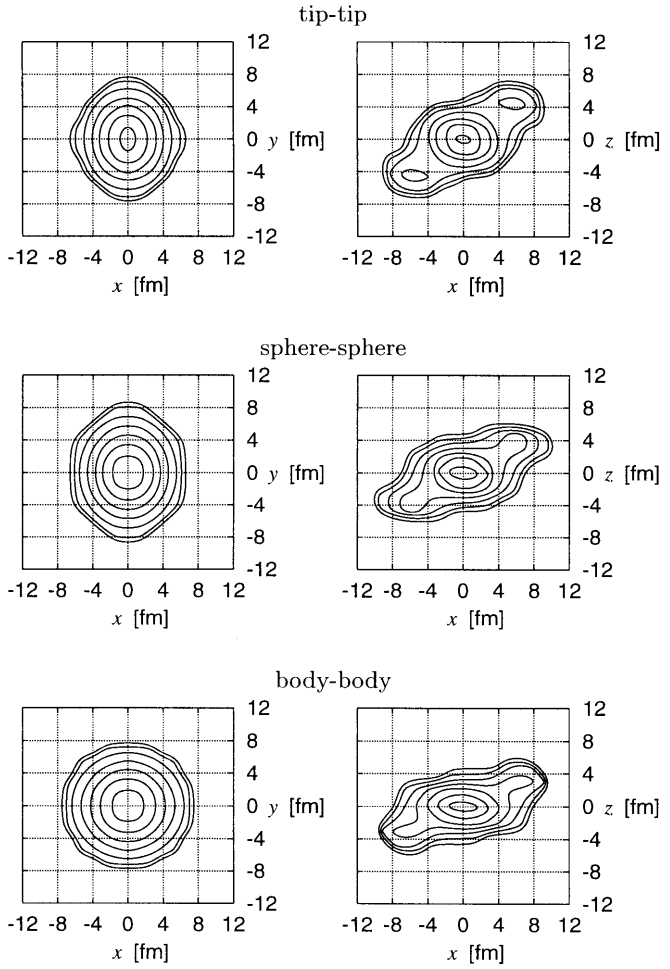

Fig. 12. The pressure distribution in tip–tip, sphere–sphere and body–body collisions of U+U 20 AGeV at $t = 20\,\mathrm{fm}/c$. The impact parameter is 4 fm in all figures. The highest value of the pressure distribution contours is $0.08\,\mathrm{GeV/fm^3}$ for all figures and the contour lines are drawn in steps of $\Delta p = 0.01\,\mathrm{GeV/fm^3}$

direction is larger than in the other cases. Therefore, v_2 in body–body collisions is less than one in sphere–sphere and tip–tip collisions at any impact parameter.

Figure 13 shows the pressure distributions at U+U 10 AGeV and U+U 20 AGeV sphere–sphere collisions at $b = 8.0\,\mathrm{fm}$. Since there is a slight difference between U+U 10 AGeV and U+U 20 AGeV in the z plane, the growth of v_2 in U+U 10 AGeV collisions is similar to U+U 20 AGeV. In the y plane the effect of the spectator in the U+U 20 AGeV case is smaller than U+U 10 AGeV. Because the effect of a Lorentz contraction becomes large for a large incident energy, the spectator becomes thin and the influence of it becomes small. Consequently, the position of the peak of v_2 (Fig. 10) moves to the large incident energy.

Here, the value of v_2, which is influenced by the deformation, is about 0.015 from Fig. 10. According to the analyses of the excitation function of the directed flow in [21,22], the flow becomes slow under the phase transition, because the speed of sound becomes small in the mixed phase, but the effect of the phase transition on the flow is expected to be small in the AGS energy region. Therefore, the effect of the deformation is significant and the value of v_2 which is obtained in this section is important. Further detailed analysis on the relation between the effect of the phase transition and the deformation on the flow may provide a new possible experimental probe of the phase transition.

4 Summary

We present (3+1)-dimensional relativistic hydrodynamical model of the Lagrangian hydrodynamics without assuming symmetrical conditions. Our algorithm is explicitly based on the entropy conservation law and the baryon number conservation law. In our algorithm we trace the volume elements of the fluid along the stream of flux. By

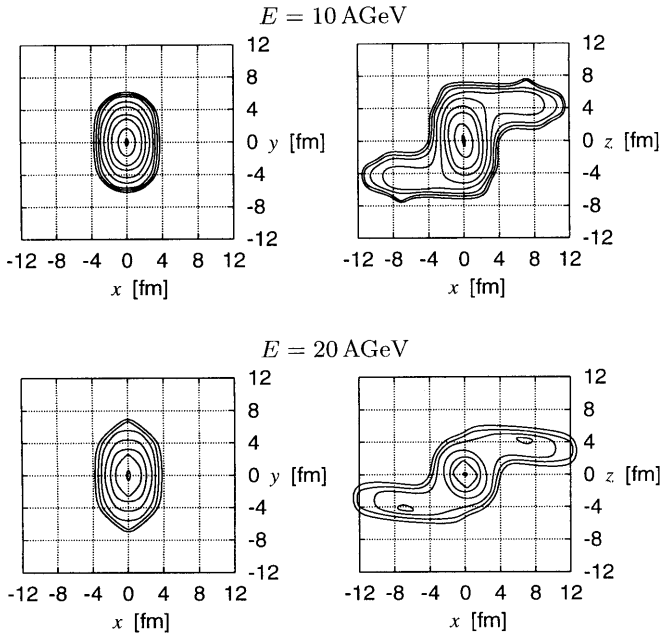

Fig. 13. The incident energy dependence of the pressure distribution in U+U 10.0 AGeV and U+U 20.0 AGeV sphere–sphere collisions at $t = 20\,\mathrm{fm}/c$. The impact parameter is 8 fm in all figures. The highest value of the pressure distribution is $0.05\,\mathrm{GeV/fm^3}$ for 10.0 AGeV collisions and $0.07\,\mathrm{GeV/fm^3}$ for 20.0 AGeV collisions. The contour lines are drawn in steps of $\Delta p = 0.005\,\mathrm{GeV/fm^3}$ for 10.0 AGeV collisions and in steps of $\Delta p = 0.01\,\mathrm{GeV/fm^3}$ for 20.0 AGeV collisions

using our relativistic hydrodynamical model based on Lagrangian hydrodynamics, the path of each volume element in the phase diagram can be traced quite easily. Therefore we can investigate directly how the phase transition takes place and affects the physical phenomena in an ultrarelativistic nuclear collision.

Using this model, we have investigated the effect of an anisotropic flow in deformed uranium collisions. The behavior of the flow depends on the pressure distribution and shadowing. Especially the shadowing effect increases with the impact parameter. As for differences in collision types, there exists only a slight difference between tip–tip collisions and sphere–sphere collisions. On the other hand, v_2 for body–body collisions is different from sphere–sphere collisions, i.e., the absolute value of v_2 is maximum at $b = 0\,\mathrm{fm}$. In light of the effect of the incident energy on v_2, the peak of v_2 is shifted to the large impact parameter region, because the shadowing effect decreases with increasing incident energy. We accordingly conclude that body–body collisions are promising for studying the nuclear equation of state and the properties of the QCD phase transition. These results are consistent with [24].

We remark the following things. In an actual experiment, a U+U collision is the superposition of different types of collisions like tip–tip, body–body, and so on. Since the contribution of body–body collisions is not negligible, v_2 does not equal zero at $b = 0\,\mathrm{fm}$. Furthermore, shadowing has a large effect on v_2.

In this paper we have applied our relativistic hydrodynamical model to the anisotropic flow. Many kinds of applications of our relativistic hydrodynamical model can be considered. Using our hydrodynamical model, we can analyze directly the phenomena which are sensitive to the phase transition. For example, we can argue how the phase transition has effects on the minimum of the excitation function of the directed flow, discussing the trajectory of a volume element of the fluid in the T–μ plane. Whether "nutcracker" phenomena can be observed in our Lagrangian hydrodynamical model is also an interesting problem. The Hanbury–Brown-Twiss effect (HBT) and the influence of anisotropic flow on HBT may also be investigated.

Acknowledgements. The authors would like to thank Prof. Osamu Miyamura for his encouragement to pursue this project and for fruitful discussions. They thank Dr. Nobuo Sasaki for providing URASiMA and useful comments. They are grateful to Prof. Atsushi Nakamura for reading the manuscript carefully. Calculations have been done at the HSP system of the Institute for Nonlinear Sciences and Applied Mathematics, Hiroshima University. This work is supported by a Grant in Aid for Scientific Research of the Ministry of Education and Culture in Japan. (No. 11440080)

References

1. For example, see the proceedings of Quark Matter '99, Nucl. Phys. A **661**, 3c (1999)
2. J. Barrette et al., E877, Phys. Rev. C **56**, 3254 (1997)
3. C. Pinkenburg et al., E895, Phys. Rev. Lett. **83**, 1295 (1999)
4. H. Appelshäuser et al., NA49, Phys. Rev. Lett. **80**, 4136 (1998)
5. A.M. Poskanzer, S.A. Voloshin for the NA49 Collaboration, Nucl. Phys. A **661**, 341c (1999)
6. M.M. Aggarwal et al., WA98, nucl-ex/9807004
7. D.H. Rischke et al., Nucl. Phys. A **595**, 346 (1995)
8. P. Danielewicz, Roy A. Lacey, P.-B. Gossiaux, C. Pinkenburg, P. Chung, J.M. Alexander, R.L. McGrath, Phys. Rev. Lett. **81**, 2438 (1998)
9. H. Sorge, Phys. Rev. Lett. **82**, 2048 (1999)
10. J.D. Bjorken, Phys. Rev. D **27**, 140 (1983)
11. Y. Akase, M. Mizutani, S. Muroya, M. Yasuda, Prog. Theor. Phys. **85**, 305 (1991); S. Muroya, H. Nakamura, M. Namiki, Prog. Theor. Phys. Suppl. **120**, 209 (1995)
12. T. Ishii, S. Muroya, Phys. Rev. D **46**, 5156 (1992)
13. J. Alam, S. Raha, B. Sinha, Phys. Rep. **273**, 243 (1996); J. Alam, D.K. Srivastava, B. Sinha, D.N. Basu, Phys. Rev. D **48**, 1117 (1993)
14. U. Ornik, M. Plümer, B.R. Schlei, D. Strottman, R.M. Weiner, Phys. Rev. C **54**, 1381 (1996)
15. J. Sollfrank, P. Huovinen, M. Kataja, P.V. Ruuskanen, M. Prakash, R. Venugopalan, Phys. Rev. C **55**, 392 (1997)
16. C.M. Hung, E. Shuryak, Phys. Rev. C **57**, 1891 (1998)
17. B.R. Schlei, D. Strottman, Phys. Rev. C **59**, R9 (1999)
18. K. Morita, S. Muroya, H. Nakamura, C. Nonaka, Phys. Rev. C **61**, 034904 (2000)
19. D. Teaney, E.V. Shuryak, Phys. Rev. Lett. **83**, 4951 (1999)

20. P.F. Kolb, J. Sollfrank, U. Heinz, Phys. Lett. B **459**, 667 (1999); hep-ph/0006129
21. D.H. Rischke, Y. Pürsün, J.A. Maruhn, H. Stöcker, W. Greiner, Heavy Ion Phys. **1**, 309 (1995)
22. J. Brachmann, S. Soff, A. Dumitru, H. Stöcker, J.A. Maruhn, W. Greiner, Phys. Rev. C **61**, 024909 (2000); J. Brachmann, A. Dumitru, H. Stöcker, W. Greiner, nucl-th/9912014
23. E.V. Shuryak, Phys. Rev. C **61**, 034905 (2000)
24. Bao-An Li, Phy. Rev. C **61**, 02193(R) (2000)
25. Ben-Hao Sa, An Tai, nucl-th/9912028
26. C. Nonaka, N. Sasaki, S. Muroya, O. Miyamura, Nucl. Phys. A **661**, 353c (1999)
27. D.H. Rischke, M.I. Gorenstein, H. Stöcker, W. Greiner, Z. Phys. C **51**, 485 (1991)
28. Particle Data Group, Eur. Phys. J. C **3**, 1 (1998)
29. L.D. Landau, E.M. Lifsitz, Fluid mechanics (Pergamon Press, Oxford 1989)
30. M. Gyulassy, K. Kajantie, H. Kurki-Suonio, L. Mclerran, Nucl. Phys. B **237**, 477 (1984)
31. S. Muroya, C. Nonaka, Bull. Tokuyama Women's College **6**, 45 (1999); nucl-th/9709004
32. A. Bohr, B. Mottelson, Nuclear structure, vol. II, p. 133 (Benjamin, New York 1975)
33. S. Daté, K. Kumagai, O. Miyamura, H. Sumiyoshi, X.Z. Zhang, J. Phys. Soc. Jpn. **64**, 766 (1995)
34. N. Sasaki, O. Miyamura, Prog. Theor. Phys. Suppl. **129**, 39 (1997)
35. N. Sasaki, hep-ph/0009326
36. F. Cooper, G. Frye, Phys. Rev. D **10**, 186 (1974)
37. U. Heinz, Nucl. Phys. A **638**, 367c (1998)
38. Jean-Paul Blaizot, Jean-Yves Ollitraut, in Quark–Gluon Plasma, edited by R.C. Hwa (World Scientific, Singapore 1990)
39. J. Ollitrault, Phys. Rev. D **46**, 229 (1992); **48**, 1132 (1993)